Research Square

Preprints are preliminary reports that have not undergone peer review.
They should not be considered conclusive, used to inform clinical practice,
or referenced by the media as validated information.

Breaking the Performance Trade-off: Unprecedented Polymer Alloys with Heterogeneously Dispersed Nanodomains via Reactive Processing

Yongjin Li

yongjin-li@hznu.edu.cn

Hangzhou Normal University

Hengti Wang

Hangzhou Normal University

Chaojie Li

Hangzhou Normal University

Ning He

Hangzhou Normal University

Toshikazu Miyoshi

University of Akron https://orcid.org/0000-0001-8344-9687

Article

Keywords:

Posted Date: March 17th, 2026

DOI: https://doi.org/10.21203/rs.3.rs-8968872/v1

License: This work is licensed under a Creative Commons Attribution 4.0 International License.
Read Full License

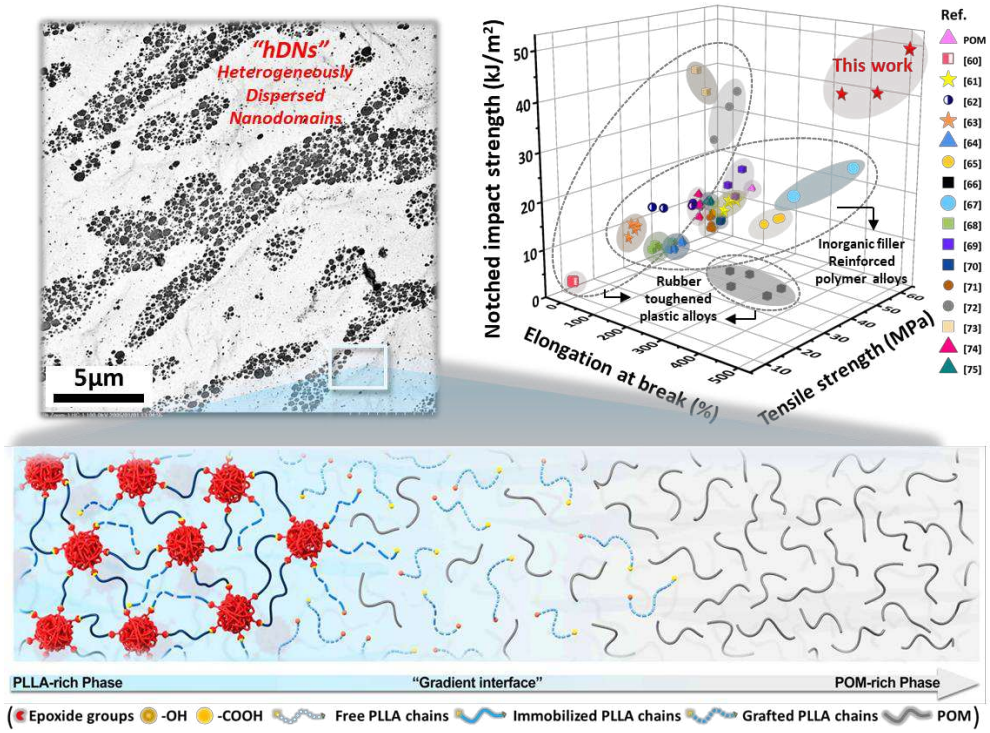
Additional Declarations: There is **NO** Competing Interest.

Version of Record: A version of this preprint was published at Nature Communications on October 20th, 2026. See the published version at https://doi.org/10.1038/s41467-026-78704-5.

Breaking the Performance Trade-off: Unprecedented Polymer Alloys with Heterogeneously Dispersed Nanodomains via Reactive Processing

Author 1 [1,2*], Author 2 [1,2], Author 3 [1,2], Author 4 [3], Author 5 [1,2*]

[1] *University A,* [2] *University B,* [3] *University C*



ABSTRACT

With over 120 million tons production annually polymer alloys that dominate the plastic market cannot satisfy all expectations owing to the persistent material-property trade-off, resulting from the limitation of structural design. We herein identify an architecturally novel microstructure that features the hitherto unprecedented phase morphology for an industrially relevant system, poly (oxy methylene) (POM)/ethylene acrylic ester-glycidyl methacrylate terpolymer (EGMA) by reactive processing, where elastomer is regionally distributed as "heterogeneously dispersed nano-domains" (hDNs) in engineering plastic matrix without a distinct interface, breaking the performance trade-off impossible to be acquired with conventional counterparts. Pre-reactive blending of EGMA with poly (L-lactide) (PLLA) and subsequent melt processing with POM plastics play orthogonal yet synergistic role in the unique morphology formation, where PLLA serving as the leveraging forces for opposing uniform distribution (keeping specific distance between hNDs regions) via chemical bonds and macro-phase separation (controlling the size of EGMA nano-domains) by physical associations. The optimal materials demonstrate a record toughness (notched impact strength, 58.6 kJ/m^2), extraordinary ductility (elongation at break, 420%), ultrahigh strength (tensile strength, 50.0 MPa), and desirable stiffness (Young's modulus, 1.3 GPa). This work identified herein innovates a totally new type of morphology for multicomponent polymers, representing a paradigm shift in narrowing gap between structure and "tailor-made" property, which endows affordable all-polymer alloys with still-unexpected combination of virtues towards pilot plant scale.

With an annual production of over 120 million of tons[1-2], polymer alloys that dominate the plastic market have become ubiquitous throughout modern society, finding widespread applications in fields such as packaging[3-4], textile[5], biomedical[6-7], to automotive[8-10], by virtue of their intriguing properties[11-13], lightweight[14], low-density[15], and re-processability[16]. Paradoxically, in most cases, owing to the persistent trade-off lies in material-performance[17-19], commodity polymer alloys commonly fail to provide desirable toughness, ductility, strength, and stiffness simultaneously, fundamentally constrains the utilizations towards emerging technologies (*i.e.* aerospace[20-21], soft electronic[22-23], unmanned aerial vehicle[24-25], and humanoid robots).

The transformative progress of advanced materials has often been accompanied by major developments in structural design at the appropriate scale[26-27]. Obviously, the aforementioned challenging lies in rational regulation of the type and dimension of heterogeneous morphology, especially for the classical rubber-toughened plastic (REP) systems. After decades of fundamental exploration, a significant effort has been made to control the microstructure of REP systems through melt processing procedure[28-30]. Following the pioneering work of Leibler and co-workers on nano-structured polyethylene (PE) /polyamide 6 (PA6) alloys by reactive blending[31], various polymer alloys with dispersed (sea-island, core-shell, and salami)[32-35], fibrillar[36], lamellar[37] and continuous[38-40] microstructure of elastomer in engineering plastic matrix have been reported. Several relations between morphology and property have been unveiled at which researchers demonstrated that droplet/matrix morphology can enhance the impact performance[41-43], fibrillar ones exhibit more beneficial to tensile properties[44-46], while the co-continuous microstructures demonstrate a particular promise for integrating advantageous characteristics of both components[47-50]. These relationships, however, give a relatively rough comparison rather than a continuously variable control at which the morphologies are independent of each other. Numerous studies exist concerning the formation mechanism of phase morphology based on the classical principles, but relatively little is known towards the correlation, transition or even combination among them. Convincing interpretation on interplay of diverse

morphologies is actively being pursued yet still remains dispiriting. On the other hand, although great advancement has been indeed established towards high-performance polymer alloys, mechanical property fails to attain quite high levels including desirable toughness (notched impact strength>50 kJ/m^2), ductility (elongation at break > 400%), favorable strength (yielding strength>50 MPa), and stiffness (Young's modulus>1.2 GPa) simultaneously, particularly regarding the non-reactive engineering plastics (*e.g.* poly (oxy methylene) (POM) due to the unfavorable interactions between multi-phases). For these reasons, it is highly anticipated to exploit architecturally novel morphology with "tailor-made" properties via existing industrial technologies.

Benefiting from the previous phase morphology, we wondered whether we could combine these classical models to target a distinct microstructure towards simultaneous maximization of mechanical performance for nowaday alloys. To this end, we herein envision and propose a de novo architectural design for an industrially relevant system, POM/ethylene acrylic ester-glycidyl methacrylate terpolymer (EGMA), by conventionally processing procedure enabled by the combinations of reactive blending of EGMA with macromolecular cross-linker and physical blending of modified EGMA (m-EGMA) with compatible engineering plastics. To do so, we introduce poly (L-lactide) (PLLA) as a leveraging force for opposing both uniform distribution of EGMA (facilitating sea-island type) and phase separation (inducing fibrillar or co-continuous categories) during processing procedure. As verified in our works very recently, *in-situ* ring-oping reaction between epoxide groups in EGMA and terminal groups in PLLA occurred during reactive processing, significantly improving the miscibility of EGMA/PLLA and controlling the droplet size of EGMA[51-53]. On the other hand, PLLA/POM demonstrates a miscible blend due to the H-bonding interactions between the carboxyl groups of PLLA and methylene groups of POM and typical lower critical solution temperature (LCST) below 230 ^{o}C[54-56]. Accordingly, combined phase morphology can be realized by balancing the well-acknowledged competition between break-up of "fragile" network facilitated by PLLA joints and immigration of PLLA towards miscible POM matrix during melt processing. As shown in **Scheme 1a**,

modified EGMA (m-EGMA) are strategically designed by reactive blending of EGMA and PLLA in the melt state. DMSA is anticipated to activate and accelerate the reaction between terminal hydroxyl groups in PLLA and epoxide groups in EGMA[57], generating dual fixation of PLLA (blue solid line) that serves as macromolecular crosslinker among EGMA. The co-existence of graft PLLA (blue dotted line) can be acquired due to the higher reactivity of terminal carboxyl groups in comparison of hydroxyl ones in PLLA. Meanwhile, excessive PLLA loadings leads to the residual free chains (light blue dotted line). Detailed *in-situ* reaction mechanism shown in **Fig. S1**.

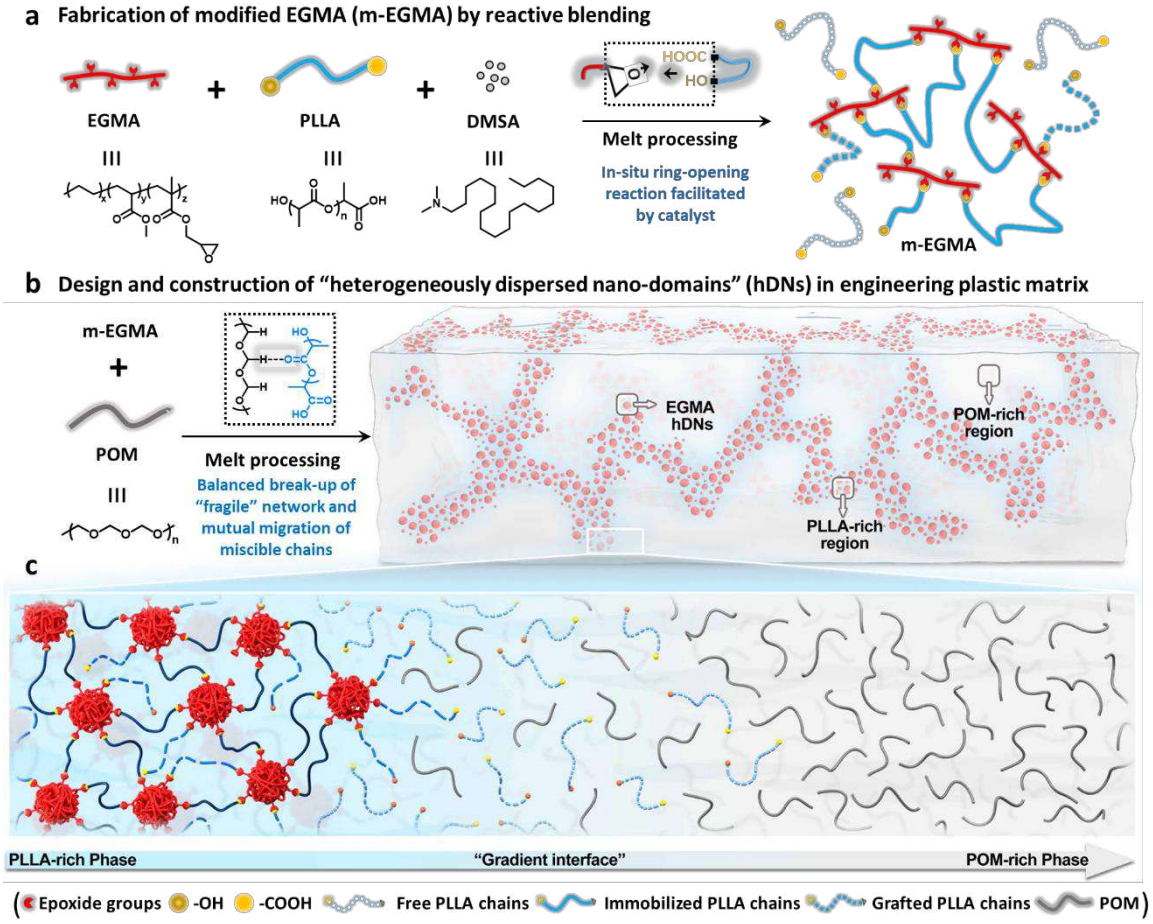


Fig. 1 | Schematic illustration of architecture design, fabrication, and formation mechanism of "heterogeneously dispersed nano-domains" (hDNs) in plastic matrix. **a** Design and preparation of modified elastomer (m-EGMA) with various topology by reactive processing between EGMA and PLLA in the molten state. DMSA serves as a catalyst for activating and accelerating the reactivity of terminal hydroxyl groups in PLLA with epoxide groups in EGMA which facilitates the formation of micro-crosslinked elastomer containing free, graft, and

immobilized PLLA chains with EGMA. **b**,**c** Schematic representation of the architectural formation of hDNs through melt processing of m-EGMA with POM. Under the shearing fields at high temperature (190 ºC), the strong non-covalent interactions between PLLA and POM chains can induce the immigration of polymer chains within plastic matrix and eventually trigger uniform distribution of EMGA nano-domains in an uneven manner in plastic matrix featuring "gradient interface".

As speculated, the immobilized PLLA chains embedded within EGMA can interfere completely coarsening and break-up of EGMA, together with stretching/migration of graft/free PLLA toward POM matrix during subsequent processing of m-EGMA with POM. A new class of polymer alloy that features exceptional distribution of rubber droplets in engineering plastics is discovered, as shown in **Scheme 1b**. Local homo-dispersion of EGMA with nanometer size spontaneously occurs due the immobilization of PLLA within EGMA, yielding engineering plastic alloys with unprecedented "heterogeneously dispersed nano-domains" (hDNs). Different from classical heterogeneous morphologies with distinct interfacial layers, hDNs elements are encompassed by "gradient interface" within engineering plastic matrix facilitated by mutual migration of miscible PLLA/POM pairs. As enlarged and illustrated in **Scheme 1c**, both PLLA and POM are penetrated throughout the whole system with gradual concentration variation in dependence of the distance from hDNs moieties to matrix, respectively. Immobilized PLLA chains occupied nano-domain region (PLLA-rich phase) while POM chains enriched matrix (POM-rich phase), in concert with the "gradient interface" containing basically identical content of PLLA (graft/free) of POM. Ultimately, the hitherto unrecognized microstructure can be steadily achieved in a synchronous manner.

Such architecturally novel morphology demonstrates an integration of conventionally independent ones, thus reflecting the optimization of property with continuously variable adjustments. Fundamental structure-performance analysis elucidated that such type of microstructure formed during processing are mainly depends on rheological behaviors, where a viscoelastic interval for the partial break-up of "fragile" network

has been established for morphological prediction. The representative hDNs structured alloys exhibit unrivalled mechanical performance including notched impact strength (58.6 ± 3.5 kJ/m^2), elongation at break (429% ± 173%), tensile strength (50 ± 1.0 MPa), and Young's modulus (1.36 ±0.02 GPa). This work provides novel insights into the morphology control of polymer alloys with ultra-tough and extremely strong characteristics in mechanical performance, stimulating the development in new-generation of valuable engineering plastic materials.

Results

Design paradigm of "heterogeneously dispersed nano-domains" (hDNs) structured polymer alloys

To begin with, a series of hDNs structured POM alloys with compositional variations of m-EGMA/POM was targeted, via two-step melt processing procedure after initial optimizing experiments (the weight ratio of EGMA/PLLA was fixed as 10/20). Comparing to the conventional counterparts with identical feed ratio in which large-scale phase separation occurs due to the strong immiscibility between EGMA and POM (**Fig. 2a**), hDNs incorporating ones conferred the distinct advantageous toward morphology such as refined droplets (from 1.75 μm to 0.23 μm, **Fig. S2**), improved interfacial interactions and local homo-dispersions (**Fig. 2b**). By tuning the feeding ratio of m-EGMA moieties in POM from 10 wt%, 30 wt%, to 50 wt% (containing 3.3 wt%, 10 wt%, and 16.7 wt% of EGMA respectively), percolated hDNs were acquired (**Fig. 2c$_1$**, **2d$_1$**). It's particular worth noting from the comparison of **Fig. 2a** and **Fig. 2c** that such a significant difference can be observed even when the content of EGMA was quite low (10wt%). SEM images providing larger-scale observation were illustrated in **Fig. S3**. Such unique morphology can be interpreted as a hierarchical combination of two distinct microstructure from classical theory, *i.e.* "sea-island" and "co-continuous". To be more specific, hDNs moieties turned into part of the independent penetrating structure featuring as co-continuous component while EGMA nano-domains in hDNs (shown dark in TEM) were uniformly distributed in the specific region familiar with droplets/matrix morphology. Moreover, as enlarged from TEM observations, while no

distinct interface can be perceived, the matrix within nano-domain region demonstrated even brighter than that without EGMA nano-domains (**Fig. 2b**$_2$, **2c**$_2$, **2d**$_2$). PLLA was reported more difficult to be stained by RuO_4 than POM[58-59], implying that a concentration gradient of PLLA should be existed in plastic matrix composed of miscible PLLA/POM pairs (detailed discussed in the following text).

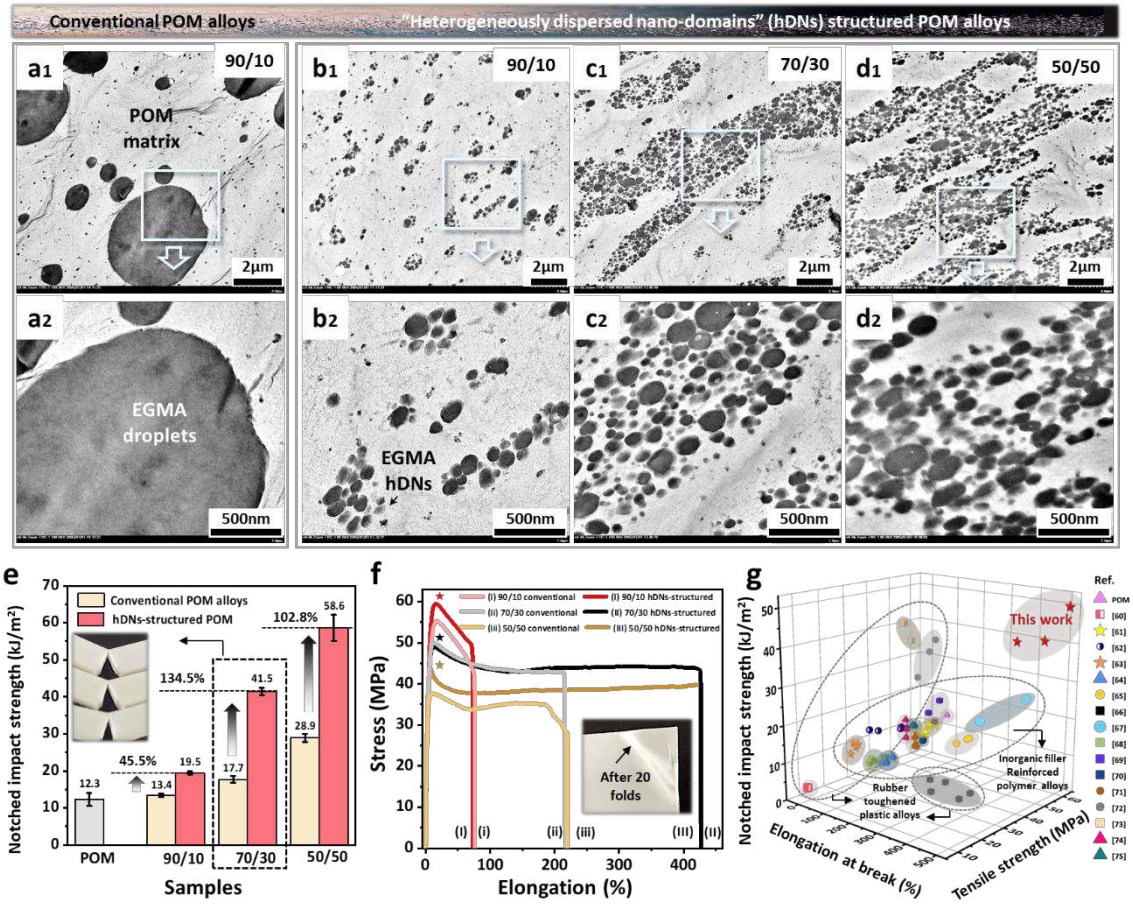


Fig. 2 | Exceptional microstructure and performance of "heterogeneously dispersed nano-domains" (hDNs) POM alloys. TEM images of **a** Conventional elastomer toughened alloys (POM/EGMA 90/10, w/w) and **b**,**c**,**d** m-EGMA incorporated alloys featuring hDNs architecture with various weight ratio of POM/m-EGMA ranging from 90/10, 70/30, to 50/50. The weight ratio of EGMA/PLLA in m-EGMA is fixed as 10/20 (w/w), and thus the content of EGMA in alloys is ranging from 3.3 wt% (90/10 alloy), 10 wt% (70/30 alloy), to 16.7 wt% (50/50 alloy). **e** Notched impact strength and **f** Representative stress-strain curves of conventional and hDNs-structured alloys. (insert) Digital photographs of the optimized alloy (hDNs, 70/30) after being impact and stretched, demonstrating its toughness and ductility, respectively. **g** 3D ashby plot of superior tensile strength, notched impact strength, and elongation at break of hDNs-structured alloys and other

reported modified POM alloys induing inorganic filler reinforced systems and rubber toughened systems as follows: POM/E-MA-GMA[60], POM/CB/NCC[61], POM/5GCE[62], POM/PTFE[63], POM/APP[64], POM/SGF[65], PLA/PCL/POM[66], POM/RCF[67], POM/PLA/EBA[68], POM/GNP[69], POM/graphite[70], POM/PEO 90/10[71], POM/MBS/TPU[72], POM/TPU[73-74], and POM/TPU irradiated[75].

The combinative morphology can obtain beneficial characteristics from both "sea-island" and "co-continuous", giving rise to the optimized performance to break the performance trade-off. Subsequently, three controls featuring refined sea-island morphology (**Fig. S4, S5**) containing identical compositions of POM/EGMA/PLLA were utilized for comparison with hDNs incorporated samples. As shown in **Fig. 2e**, hDNs-structured alloys demonstrated tremendous advantages over the controls in terms of notched impact strength: 10 wt% (13.4 ± 0.5 *vs* 19.5 ± 0.4 kJ/m^2), 30 wt% (17.1 ± 09 *vs* 41.5 ± 0.9 kJ/m^2), 50 wt% (28.9 ± 1.1 *vs* 58.6 ± 3.5 kJ/m^2), representing a huge leap of 45.5%, 134.5%, and 102.8% compared to conventional alloys. SEM images after notched impact tests demonstrated the ultra-toughness of hDNs-structured alloys, as shown in **Fig. S6**. Moreover, it is worth noting from the tensile properties that the improvement brought about by the unprecedented microstructure had no negative effects on the compromise of mechanical strength. The optimal alloys incorporating hDNs moieties showed desirable stretchability (elongation at break 429 ± 173%), extraordinary stiffness (tensile strength 50 ± 1.0 MPa), and ultrahigh rigidity (Young's modulus 1.36 ± 0.02 GPa) (**Fig. 2f**, detail listed in **Table S1**). This distinguished the proposed strategy from the traditional method for toughening/reinforcing engineering plastics by increasing content of elastomer/inorganic filler, which inevitably at the expense of lower toughness/stiffness, acknowledged as a persistent trade-off in materials. The mechanical performance of hDNs-structured alloys was also compared with reported polymer alloys including inorganic filler reinforced systems and rubber toughened systems[60-75]. As illustrated in **Fig. 2g**, in terms of notched impact strength, elongation at break and tensile strength, our works demonstrated striking advantages beyond conventional plastic alloys, which we believe to be directly correlated the contribution of local homo-dispersion and "gradient interface" in our hDNs-structured

alloys (Detail listed in **Table** S2). The pronounced variation can be further verified from rheological behaviors, as shown in **Fig.** S7, S8. Overall, it can be revealed that the novel architecture played a decisive role in determining the performance of plastic alloys. hDNs (70/30) alloy herein exhibited balanced and optimized performance towards ultra-toughened and extremely strong plastic alloys, and thus it was selected as the representative one for the subsequent investigation.

It's interesting to obtain such a unique morphology via traditional reactive processing procedure. For an insight into architectural analysis, Nano-IR of conventional alloy and the representative hDNs-structured one was subsequently conducted.

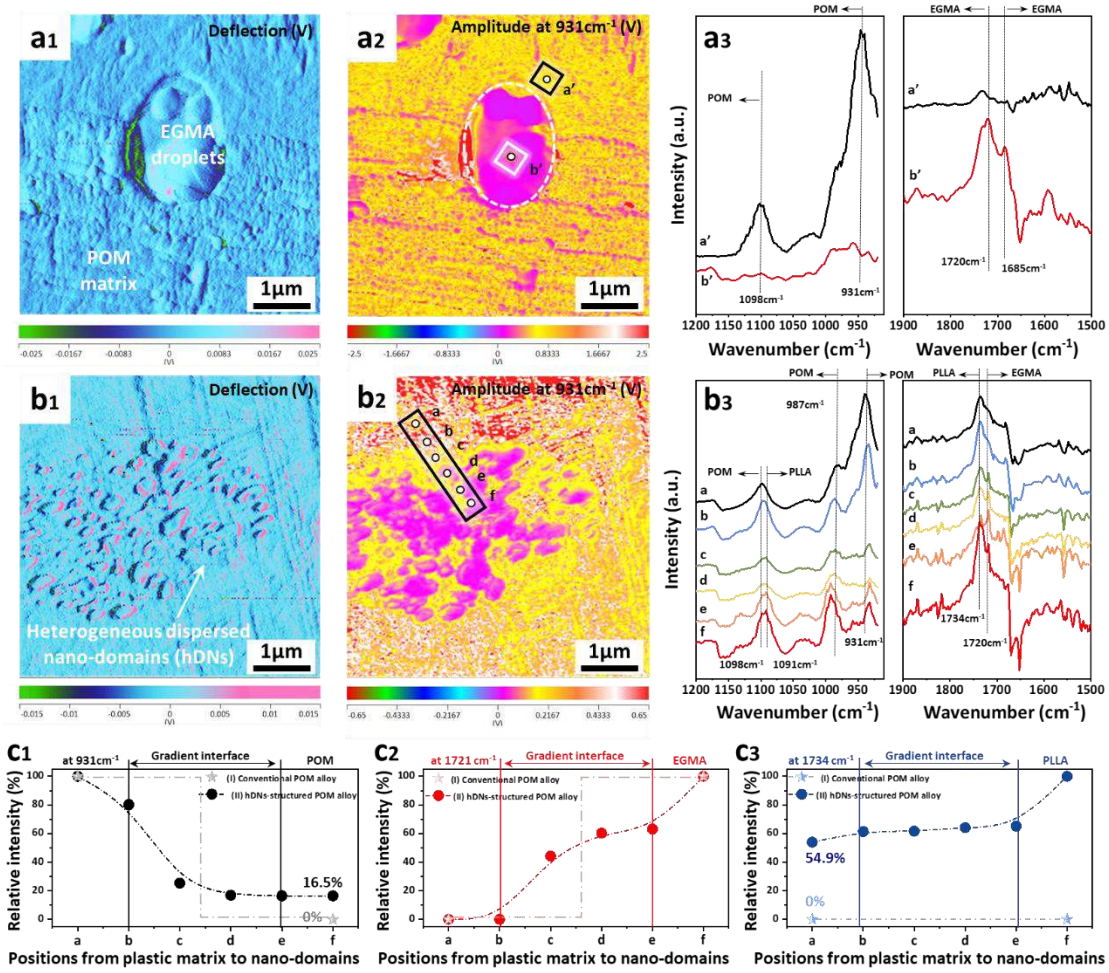


Fig. 3 | AFM height image, Nano-IR images scanned at 931 cm^{-1}, and IR spectra acquired at points with various locations of **a** Conventional elastomer toughened POM alloy, **b** hDNs-structured POM alloy recorded by nano-IR. The two alloys mentioned above contains identical content of EGMA moieties at 10 wt%. **c** Relative intensity of characteristic peaks of POM alloys calculated from nano-

IR spectra: $\mathbf{c_1}$, 931 cm^{-1}, $\mathbf{c_2}$, 1720 cm^{-1}, and $\mathbf{c_3}$, 1734 cm^{-1} assigned to POM, EGM, and PLLA, respectively.

Fig. 3a represented the AFM (**Fig. 3a$_1$**) and nano-IR (**Fig. 3a$_2$**) images of POM/EGMA (90/10) laminate (100 nm) featuring conventional droplets/matrix morphology. Note that nano-IR images were scanned at the wavenumber of 931 cm^{-1}, which was specific for $\nu_{(C\text{-}O\text{-}C)} + \omega_{(CH_2)}$ in POM. In this case, the nano-IR image demonstrated a distinct boarder between EGMA droplets (indicated in red) and POM (indicated in yellow), implying that no mutual diffusion or migration occurred owing to the high interfacial tension between them. It can be further confirmed by the representative all recorded IR spectroscopy at different positions (**Fig. 3a$_3$**), where neither EGMA-specific peak observed in POM matrix (Curve a', shown in black) nor POM-specific peak in EGMA region (Curve b', shown in red). In a striking contrast, the situation changed remarkably for the hDNs-structured alloys. AFM and nano-IR images in **Fig. 3b** implied that both POM and PLLA segments co-existed throughout nano-domain without sharp boarder due to the mutual diffusion of miscible polymer chains during melt processing, as indicated by the frame line and the corresponding spectroscopy. Such hDNs moiety can be defined as the area where the all polymers can be detected, exhibiting POM specific (1098 cm^{-1}, 987 cm^{-1}, 931 cm^{-1}), PLLA specific (1091 cm^{-1}, 1734 cm^{-1}), and EGMA specific (1721cm^{-1}). The pristine FT-IR spectra of the three components were shown in **Fig. S9**. It can be strongly verified from the positional scans that there is a concentration gradient of polymer components, as shown in **Fig. 3b$_3$**. The normalized height of C-O-C stretching vibrations at 1098 cm^{-1} (ether bond) and C-O-C stretching vibration (ester bond) at 1091 cm^{-1}, for instance, can be taken as a measure of POM and PLLA contents across the hDNs region. The intensity of PLLA was highest within nano-domain area, where that for POM was lowest (**Curve f**, shown in red). As anticipated, the intensity of the latter was similar to that of the former (**Curve c**, shown in green) and gradually increase towards plastic matrix (**Curve a**, shown in black). This result supports the supposed "gradient interface" of POM/PLLA contents due to the miscibility. For better comparison, the relative intensity of characteristic peaks associated with POM (931 cm^{-}

$^{-1}$), EGMA (1721 cm^{-1}), and PLLA (1734 cm^{-1}) as a function of location have been calculated and shown in **Fig. 3c**. Different from the conventional alloy displaying distinct interface between POM and EGMA (visualized by dotted line), gradual variation of concentrations of POM (reducing trend, **Fig. 3c$_1$**) and EGMA (rising trend, **Fig. 3c$_2$**) can be observed with the prolonging of the distance from plastic matrix to nano-domain region (from point a to d). Notably, POM components still existed in hDNs region containing 16.5% of relative intensity. Similar phenomenon can be observed for PLLA (54.9% of intensity), as shown in **Fig. 3c$_3$**. Nano-IR measurements provided an intuitive and quantitative insight into the formation of "gradient interface" surrounding hDNs, which is first characterized and visualized to the best of our knowledge.

Fundamental structure-performance characterizations of polymer alloys with "heterogeneously dispersed nano-domains" (hDNs)

In the preceding section, we have presented the remarkable enhancement in the mechanical performance of hDNs-structured alloys mainly originating from the penetrated nano-domain moieties and "gradient interface". However, we still curious about the roles of PLLA, including inner crosslinker and outer graft/free PLLA chains of EGMA in the morphological formation, and why they were serving as leveraging forces for opposing uniform dispersion and macro-phase separation of EGMA within miscible PLLA/POM matrix during melt processing? To clarify these issues, in the following sections, we further designed and fabricated various samples of which the topology of m-EGMA was regulated to comprehend the break-up of "fragile network", while compositional ratio was further accommodated to evaluate the mutual diffusions of the miscible pair chains between PLLA and POM.

Crosslinking density dependence of m-EGMA in hDNs-structured alloys

As mentioned previously, hDNs (70/30) alloy which possessed the optimized and balanced mechanical properties was selected as the representative sample for subsequent investigation. Various crosslinking density of m-EGMA with identical composition (EGMA/PLLA=10/20, w/w) were obtained by regulating the

concentration of DMSA catalyst, where the gel content increased from 0% (0DMSA), 13.8% (0.3DMSA), 18.6% (0.6DMSA), 25.9% (1.2DMSA), to 29.9% (2.4DMSA), as depicted in **Fig. 4a**. The inserted TEM images of m-EGMA with or without DMSA provided direct evidence that the acceleration of reactivity owing to catalyst makes a contribution of the refined dispersion of EGMA in PLLA. More characterization including torque variations during melt processing, FT-IR, TGA after selective extraction of free chains, and TEM with various magnifications were shown in **Fig. S10-S13, Table S3**. Small amplitude oscillatory shear (SAOS) experiments were further conducted to explore the rheology behaviors of POM, conventionally graft elastomer (0DMSA) and the crosslinked m-EGMA.

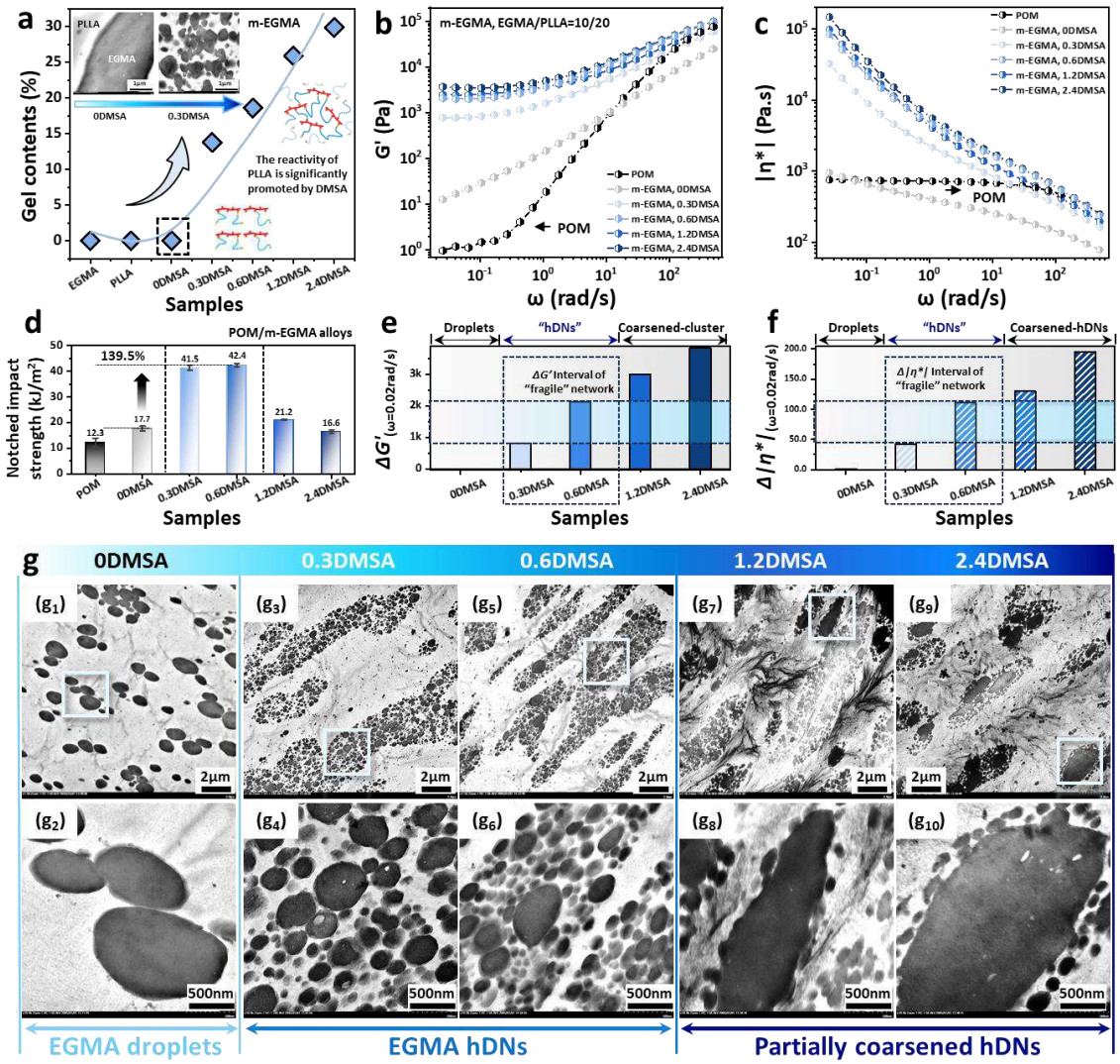


Fig. 4 | Architecture and performance of hDNs-structured alloys incorporating various crosslinking density of m-EGMA. **a** Gel contents **b** Storage modulus (*G'*) and **c** Complex viscosity

($|\eta^*|$) against shifted angular frequency (ω) of m-EGMA with different concentration of DMSA ranging from 0 wt%, 0.3 wt%, 0.6 wt%, 1.2 wt%, to 2.4 wt%. **d** Notched impact strength values of the POM/(EGMA/PLLA) 70/(10/20), w/(w/w) alloys. Corresponding ratio statistics values of **e** $\Delta G'$ of $G'_{(m\text{-}EGMA)}$ / $G'_{(POM)}$ and **f** $\Delta|\eta^*|$ of $|\eta^*|_{(m\text{-}EGMA)}/|\eta^*|_{(m\text{-}EGMA)}$ acquired at low angular frequency (ω=0.02 rad/s). The weight ratio of EGMA/PLLA is fixed as 10/20. **g** TEM images of POM/(EGMA/PLLA) 70/(10/20) w/(w/w) alloys with different content of DMSA.

As illustrated in **Fig. 4b** and **Fig. 4c**, upon addition of 0.3DMSA catalyst, $G'_{(\omega)}$ and $|\eta^*|_{(\omega)}$ values were elevated by two orders of magnitude for the m-EGMA, as compared with the linear elastomer (0DMSA). The frequency-independent plateau appeared more pronounced with the further increasing of DMSA, implying pseudo solid-like response in terminal region[76-77]. Obviously, the gradually retarded terminal relaxation phenomenon can provide intuitive evidence of the formation of denser network structure within m-EGMA via elevating catalyst loading[74-75]. Meanwhile, it was noteworthy that both the $G'_{(\omega)}$ and $|\eta^*|_{(\omega)}$ values of POM were almost two orders much lower than that of m-EGMA within the whole range of ω investigated. It was well-recognized in classical principle that the type and size of phase morphology, formed during melt blending, were mainly dependent on the ratio of viscoelasticity between phases (This issue will be emphasized and discussed in detail below)[76-77]. The topological variation of m-EGMA brought about a significant change of mechanical performance, as shown in **Fig. 4d**. A tremendous improvement of impact property can be realized for the alloys containing m-EGMA with moderate crosslinking density, where a great leap of 139.5% in notched impact strength was obtained for 0.3DMSA incorporated alloy (41.5 kJ/m^2) compared to 0DMSA one featuring graft topology. Detailed characterizations of performance including tensile tests and related parameters were shown in **Fig. S14** and **Table S4**. It was demonstrated that the catalyst can significantly enhance the immobilization of PLLA onto EGMA and improve the integrity of network within m-EGMA, thereby bestowing the plastic alloys with "tailor-made" property even when the content of all components was constant.

To comprehensively explore the correlation between the inner network of EGMA and

hDNs microstructure, quantitative rheological analyze were carried out. The viscoelastic ratios of POM matrix and m-EGMA component were estimated by the equations 1 and 2, and displayed in **Fig. 4e**, **4f**.

$$\triangle G'_{\omega} = \frac{G'_{\omega(m-EGMA)}}{G'_{\omega(POM)}} \quad (1)$$

$$\triangle |\eta^*_{\omega}| = \frac{|\eta^*_{\omega(m-EGMA)}|}{|\eta^*_{\omega(POM)}|} \quad (2)$$

Here $G'_{\omega(m-EGMA)}$ and $G'_{\omega(POM)}$ referred to the storage modulus of m-EGMA and POM, $|\eta^*_{\omega(m-EGMA)}|$ and $|\eta^*_{\omega(POM)}|$ referred to the complex viscosity of m-EGMA, and POM, respectively. For better comparison, we chose the SAOS data in the low ω region since the discrepancy in fluid dynamic behavior turned more pronounced at terminal region. The ideal formation of hDNs architecture can only be obtained in a narrow interval of rheological ratio, as highlighted with blue in statistical data. The structural variations brought by the viscoelastic discrepancy during melt processing were also supported by TEM (**Fig. 4g**) and SEM characterizations (**Fig. S15**). In the case of m-EGMA without network (0DMSA), conventional sea-island morphology incorporating coarsened elastomeric at micrometer scale can only be obtained (**Fig. 4g$_{1-2}$**). This was mainly originated from the excessively low value of rheological ratio, thus the self-similar coarsening process was dominant beyond filament break-up under high shearing field during melt blending[78-79]. By contrast, a coarsened-domain morphology where limited nano-domain surrounded exterior surface of EGMA droplets was observed for the alloys containing high crosslinking density of m-EGMA **(Fig. 4g$_{7-10}$)**. It was reasonable that the break-up of m-EGMA was significantly suppressed due to the existence of solid network in m-EGMA, quantitatively reflecting on the quite high levels of viscoelastic ratio (**Fig. 4g$_{3-6}$**). As a consequence, desired hDNs structure containing refined nano-domains can be realized, as the ratio lies between the two limits. We speculate that the intermediate m-EGMA with moderate content of immobilized PLLA chains were deemed as a "fragile" network to be partially cracked under shearing fields, thus implanting favorable hDNs microstructure into alloys.

Composition dependence of m-EGMA in hDNs-structured alloys

On the other side, to better elucidate the role of graft/linear PLLA chains in facilitating the formation of "gradient interface", we also designed and fabricated a series of samples containing various contents of PLLA in m-EGMA (weight ratio of EGMA/PLLA ranging from 10/1,10/3, 10/5, 10/10, 10/15, 10/20, 10/25, to 10/30) under a prerequisite of fixed loading of DMSA (0.3wt%) and identical EGMA concentration in the final alloys (10 wt%).

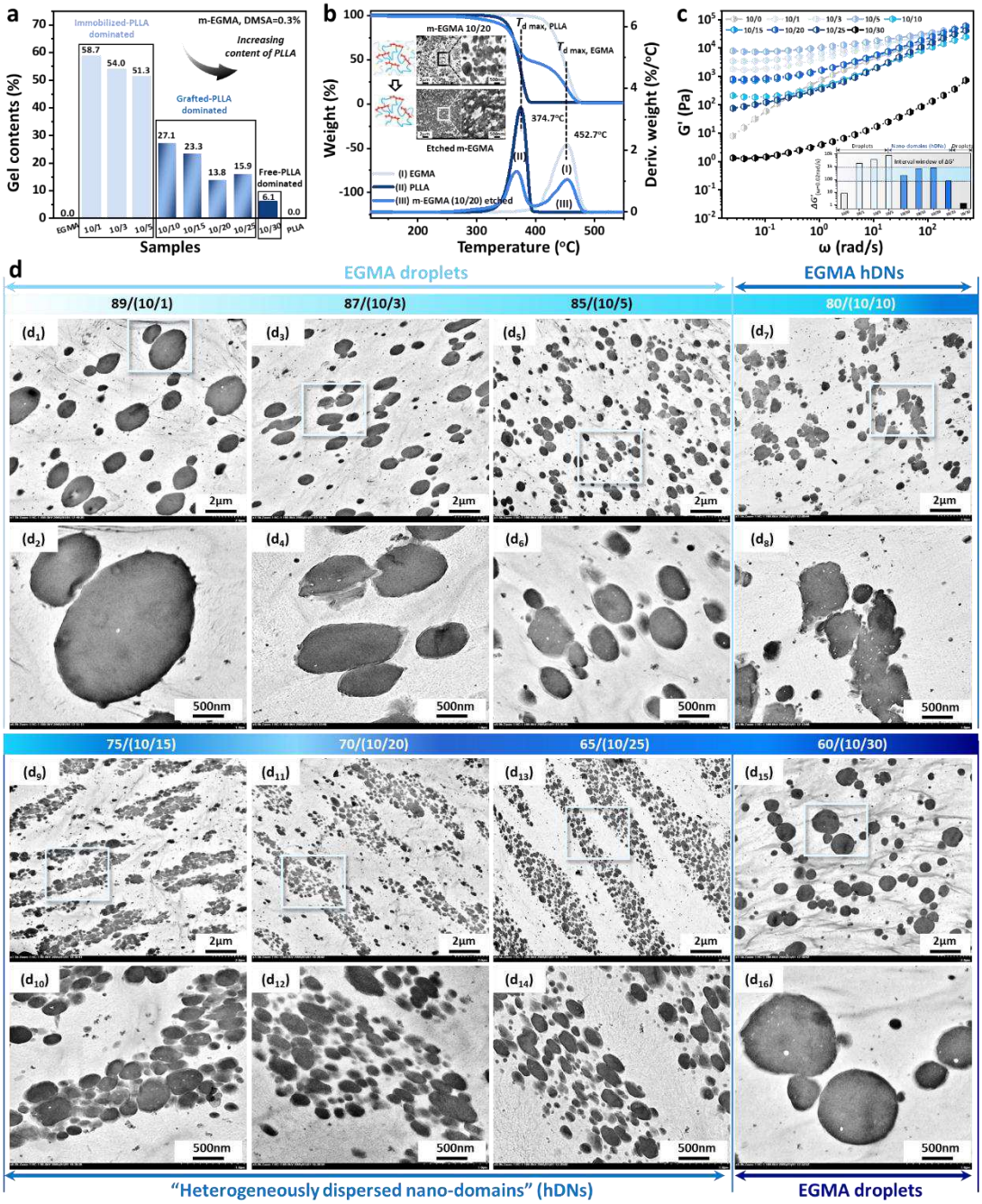


Fig. 5 | Architecture and performance of hDNs-structured alloys incorporating various compositional ratio of PLLA in m-EGMA. **a** Gel contents of m-EGMA with various weigh ratio of EGMA/PLLA. **b** TGA thermograms of EGMA, PLLA, and m-EGMA (EGMA/PLLA10/20) after selectively extraction of free PLLA chains via chloroform, (insert) TEM images of m-EGMA (EGMA/PLLA10/20) before and after extraction. **c** Storage modulus (G') of m-EGMA, (insert) corresponding statistics data in ratio values of $\Delta G'$ acquired at ω=0.02 rad/s. **d** TEM observations of POM/(EGMA/PLLA) alloys containing identical EGMA loading (10 wt%). The concentration of DMSA is fixed as 0.3 wt%.

In detail, three types of m-EGMA with distinct topology, termed as "immobilized-PLLA dominated", "graft-PLLA dominated", and "free-PLLA dominated" elastomer, were selected to serve as the controls demonstrating various migration capacity toward POM during processing by regulating feed ratio of PLLA in the pre-reactive blending procedure. For the structure of "immobilized-PLLA dominated", almost all PLLA have been dually bonded onto EGMA chains (from 10/1 to 10/5), the macromolecular crosslinkers thereby resulting in the significant enhancement of gel content (51.3%-58.7%), as verified and shown in **Fig. 5a**. As for the second category m-EGMA, we exploited the "graft-PLLA dominated" containing more dangling chains in comparison of immobilized joints and free chains PLLA by increasing of PLLA component. Note that the stoichiometry of PLLA was excessive beyond EGMA within this range of feeding ratios (from 10/10, 10/20 to 10/25), resulting in the predomination of grafting reactions facilitated by the terminal carboxyl groups in the excess PLLA chains which demonstrated much higher reactivity than hydroxyl groups[57]. Accordingly, the gel content was significantly reduced (13.8%-27.1%) owing to the excessive content of graft and liner PLLA chains. The gel content was notably decreased to 6.1% with the further increasing of PLLA (10/30) for the third type of m-EGMA. It was reasonable that abundant PLLA chains with linear topology was brought into the binary system, inducing the "free-PLLA dominated" m-EGMA. **Fig. 5b** illustrated the TGA results of the representative m-EGMA (10/20) after selectively extraction of free chains. It can be observed that almost identical content of EGMA and PLLA were preserved even though

the dosage of PLLA was quite excessive (**Curve III**), implying the co-existence of free PLLA chains in "graft-PLLA dominated" m-EGMA. More evidence can be found from TEM results of m-EGMA before and after selective extraction, as shown in **Fig. S16**. The difference of aforementioned three types of m-EGMA were further characterized by rheological experiments, as illustrated in **Fig. 5c**. The terminal plateau corresponding to inner elastic network structure turned more pronounced in "immobilized-PLLA dominated" than that for "graft-PLLA dominated", and dropped dramatically for "free-PLLA dominated" ones, which was consistent with the previous inference. Subsequently, the mechanical performance of the alloys containing various kind of m-EGMA were characterized by impact and tensile tests as demonstrated in **Fig. S17**, **Fig. S18, Table S5**. Except for similar ductility with high elongation at break, "graft-PLLA dominated" incorporated alloys displayed enormous advantages over the other two categories in terms of notched impact strength (41.5-43.3 kJ/m^2). Such notable disparity in toughness inferred that the additional introduction of graft PLLA played a decisive role in the formation of the unforeseen nanodomain heterogeneity in hDNs, thus greatly improving the comprehensive performance. In addition, "free-PLLA dominated" m-EGMA seemed to having a deteriorating effect on mechanical property. A series of rheological estimations (**Fig. 5f**) and morphology observations (**Fig. 5d**) were further conducted to take an in-depth insight into the correlation of structure-performance of our m-EGMA incorporated alloys. As depicted in **Fig. 5d**, the phase morphology was directly determined by m-EGMA, ranging from droplet/matrix ("immobilized-PLLA dominated"), nano-domain enriched ("graft-PLLA dominated"), to droplet/matrix ("free-PLLA dominated") microstructure. The architectural evolution (SEM images, detail statistic data and thermal behaviors of the alloys were shown in **Fig. S19-S22**) was associated with the viscoelastic behaviors, whereas the distinguishing hDNs morphology were formed within the rheological interval region with identical EGMA loading. Reasonably, we speculate that besides the partially suppressed break-up brought by the inner "fragile" network of m-EGMA, the effective interactions resulting from the stretching of dangling PLLAs towards POM matrix also

functioned as crucial role in determining the final morphology. The existence of graft PLLAs can not only suppressed the aggregation of elastomer owing to the inner immobilized PLLAs (shown in **Fig. 5d**$_{1\text{-}6}$), but also avoid complete stretching and migration of remaining free PLLAs due to the strong interactions of miscible PLLA/POM pair (illustrated in **Fig. 5d**$_{15\text{-}16}$). The estimated data of viscoelastic difference provided a prediction of quantitative range, figuring out the equilibrium point where similar-like coarsening and entire break-up of "fragile" network were balanced.

With the purpose of better exhibiting the mechanical performance, hDNs incorporated engineering plastic alloys integrated more content of elastomer has been designed and fabricated. Based on the prediction model established above, various m-EGMA within the theoretical range of rheological parameters were constructed and incorporated into POM. The tensile and impact experiments were conducted as shown in **Fig. 6a-b**.

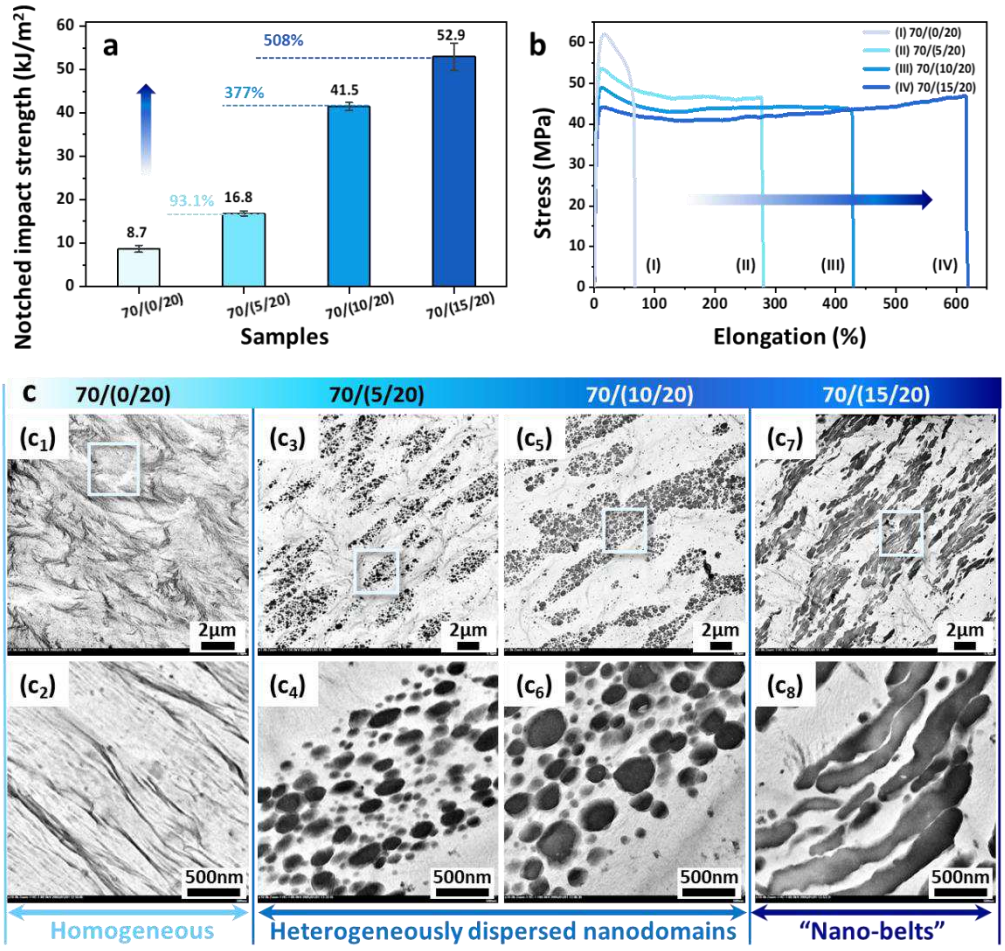


Fig. 6 | Architecture and performance of hDNs-structured alloys incorporating various

compositional ratio of EGMA in m-EGMA. **a** Notched impact strength values, **b** Representative stress-strain curve, and **c** TEM observations of POM/(EGMA/PLLA) alloys containing identical PLLA loading (20 wt%). The concentration of DMSA is fixed as 0.3 wt%.

The results suggested that both the toughness (an immense leap of 508% from 8.7 to 52.9 kJ/m^2) and ductility (a significant enhancement from 67.9% to 619.5%) increased with the further addition of EGMA in hDNs element (SEM images and detailed mechanical parameters are shown in **Fig. S23, Table S6**). More interestingly, elongated elastomeric nano-belts can be observed for the alloys containing 15 wt% of EGMA (**Fig. 6c**$_{7\text{-}8}$). Such novel morphology seemed as a hierarchical combination of "co-continuous" and fibrillar morphology in which nano-belt moieties penetrated within plastic matrix featuring as percolating component while EGMA were oriented in hDNs regions familiar with fibers of EGMA. As a consequence, intriguing integration of advantageous performance can be realized via melt processing which is pursuing for long time by scientists.

Insight into the formation mechanism of "heterogeneously dispersed nano-domains" (hDNs) microstructure upon melt processing

It is interesting to obtain a totally new type of morphology for an industrial relevant POM-based system via reactive processing, which exhibited the tremendous improvement in mechanical performance that could not be acquired with traditional polymer alloys, neither rubber-toughened nor inorganic filler-reinforced systems. In this section, the morphological evolution of heterogeneously dispersed nanodomains was investigated. Due to the complex interdependence during melt processing, various parameters such as interfacial tension, viscosity and elasticity should be taken into consideration. We mainly focused on the intrinsic complex of m-EGMA introduced naturally by the reactive processing procedure. As designed and clarified earlier in this article, three types of PLLAs, including immobilized (macromolecular crosslinker), dangling (graft segments), and linear (free chains), were generated in m-EGMA via one-pot reactive blending. They could play orthogonal yet synergistic roles to maintain and stabilize the exceptional morphology after the subsequent melt mixing with POM.

The details are illustrated as follows and shown in **Fig.** 7.

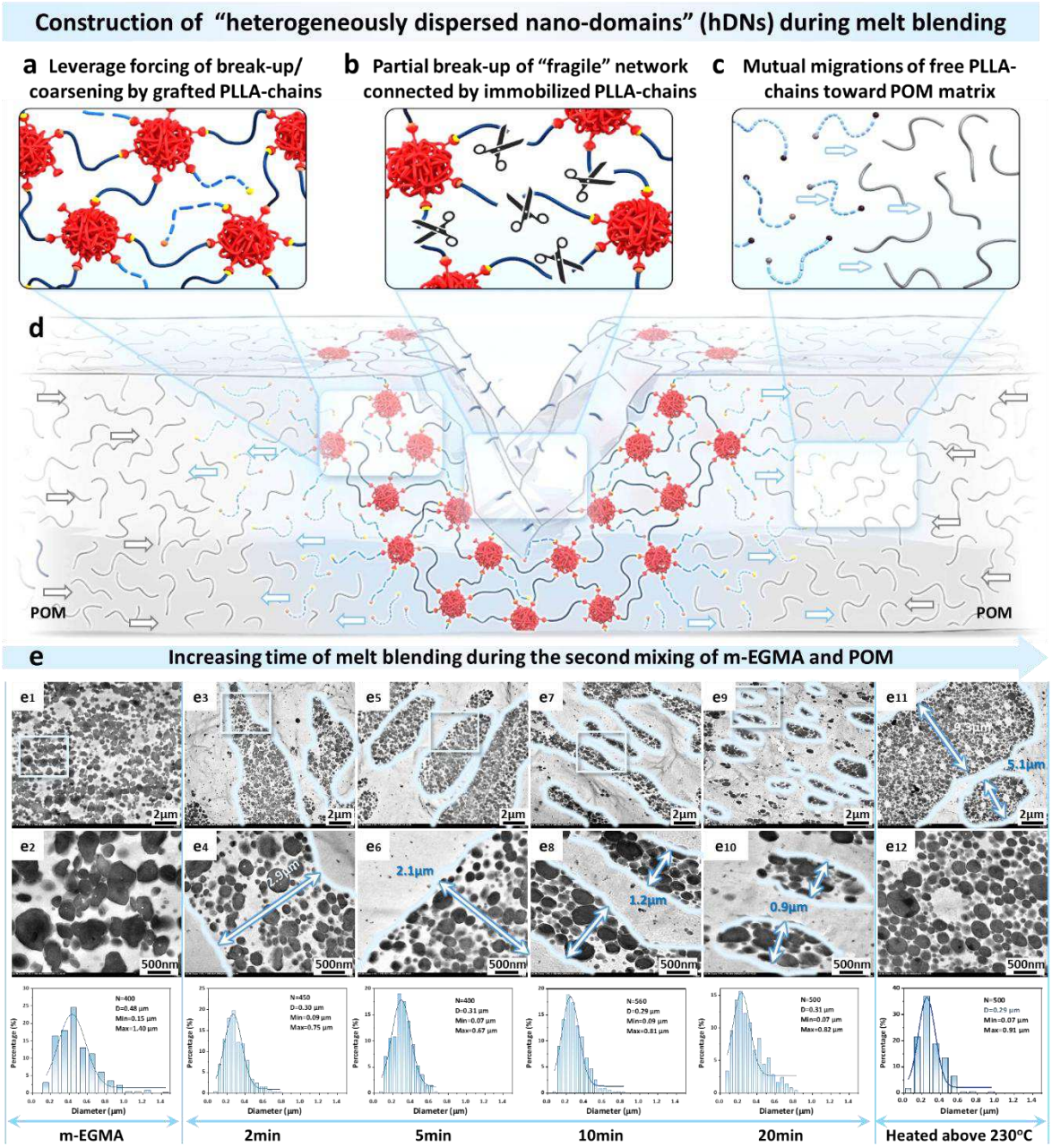


Fig. 7 | a,**b**,**c**,**d** Schematic diagram of morphology development mechanism of "heterogeneously distributed nano-domains" (hDNs) microstructure in engineering plastic matrix during melt processing. **e** Corresponding TEM observations of $\mathbf{e_1}$, $\mathbf{e_2}$ m-EMGA (EGMA/PLLA 10/20), and POM/(EGMA/PLLA) 70/(10/20) alloys captured at different processing times at 190 °C with a rotation speed of 50 r/min: $\mathbf{e_3}$, $\mathbf{e_4}$ 2 min, $\mathbf{e_5}$, $\mathbf{e_6}$ 5 min, $\mathbf{e_7}$, $\mathbf{e_8}$ 10 min and $\mathbf{e_9}$, $\mathbf{e_{10}}$ 20 min, and $\mathbf{e_{11}}$, $\mathbf{e_{12}}$ heated above 230 °C.

As demonstrated in **Fig.** 7**a-d**: (I) The inner dual joints of PLLA onto EGMA facilitated

a “fragile” network within m-EGMA, which can be partially cracked upon high shearing force in melt state. As highlighted in **Fig. 7b**, balanced coarsening/break-up of m-EGMA occurred, contributing to the local homo-dispersion of EGMA as hDNs in the miscible plastic matrix. (II) Due to the LCST (below 230 °C) phase behavior of POM/PLLA, mutual migrations of free PLLAs toward POM spontaneously occurred during melt processing at 190 °C (highlighted in **Fig. 7c**). Therefore, the exterior PLLA chains in m-EGMA can not only facilitate the dispersion of nano-domains with nanometer size, but also induce the “gradient interface” in this system. (III) The dangling PLLAs via grafting reaction between terminal carboxyl groups of PLLA and epoxide groups of EGMA served as the leverage force for opposing uniform dispersion (keep specific distance between nano-domain) and macro-phase aggregation (control the droplet size of EGMA). As demonstrated in **Fig. 7a,d**, PLLA grafts were located between the inner joints and exterior free PLLA chains. On the one hand, improved interactions between m-EGMA and immiscible POM/PLLA was realized due to the stretching of dangling PLLAs towards plastic matrix. On the other hand, entire migration of free PLLAs, which led to self-similar coarsening, was significantly distracted by virtue of dangling PLLAs.

To better clarify the kinetic process during melt blending, morphological observations was further performed for the representative hDNs-structured alloy(70/30) (discussed in **Section 2.1**) captured with different processing times and illustrated in **Fig. 7e**, **Fig. S24**. As demonstrated, break-up of “fragile network” occurred upon 2 min of mixing, accompanied with the remarkable reduction of droplet size of EGMA from 0.48 μm to 0.30 μm. It was reasonable since the competition among retraction, break-up and coarsening of m-EGMA was predominant in initial stage[41-43, 80-81]. With the prolonging time of mixing from 2 min to 10 min, a gradual transition of hDNs from aggregates to finely percolated nano-domain phase was observed: the dimension of hDNs components decreased from 2.9 μm (2 min), 2.1 μm (5 min), to 1.2 μm (10 min). After 20 min of compounding, dissociation of continuous hDNs occurred due to the deterioration of “fragile” network. Obviously, the size reduction of hDNs may come

from the increasing interchain penetrations between PLLA and POM with increasing time of mixing. This speculation can be verified by the subsequent coarsening of hDNs upon heated up to 230 ^{o}C, as shown in **Fig. 7e$_{11}$-e$_{12}$**. According to the LCST behavior, phase separation between PLLA and POM occurred at higher temperature (above 230 ^{o}C), and thereby led to the formation of large-scale aggregations of hDNs (5.1 μm-9.3 μm). From another perspective, it was interesting to find that the size of each EGMA droplet remained unchanged as a function of processing time. We believe that this phenomenon was directly related to the moderate content of immobilized PLLA in m-EGMA. Overall, the "fragile" networks within m-EGMA can interfere entirely coarsening/break-up of EGMA against shearing fields, yielding local homo-dispersion of elastomer featuring as hDNs element. Moreover, the coexistence of graft/free motifs can synchronously migrate toward POM owing to the strong miscibility between PLLA and POM in the melt state, thereby affording the hitherto unrecognized hDNs microstructure encapsulated by "gradient interface" within miscible plastic matrix.

Discussion

We introduce a designing criterium in constructing the structurally novel "heterogeneously dispersed nano-domains (hDNs)" microstructure in engineering plastic matrix featuring "gradient interface" by virtue of pre-reactive blending of EGMA with PLLA and the subsequent physical blending of modified EGMA (m-EGMA) with POM plastics, where PLLA is reactive with EGMA while miscible with POM through reactive processing. Unlike previous approaches that concentrate solely on classical morphologies which are independent of each other, our method combines and optimizes these classical models to exploit a distinct morphology, endowing the obtained plastic alloys with unrivalled performance to break the performance trade-off that hitherto impossible to be acquired with conventional engineering plastic alloys. Strategic variations of topology, feed ratios, and processing conditions allowed for adjustable phase morphology, conferring record toughness (notched impact strength 58.6 kJ/m^2), along with extraordinary ductility (elongation at break>420%), and ultrahigh stiffness (tensile strength 50>MPa). We elucidated the triple effects of m-

EGMA, featuring immobilized (macromolecular crosslinker), dangling (graft segments), and linear (free chains), in opposing uniform dispersion (keep specific distance between nano-domain) and macro-phase segregation (control the droplet size of EGMA), revealing the formation mechanism of hDNs microstructure. Rheological estimations have been further explored, enabling quantification and prediction of hDNs microstructure with regard to industrially relevant protocols.

In summary, our ultra-tough and extremely strong alloys are an ideal replacement for existing engineering plastic alloys that demonstrates a great potential in versatile applications ranging from daily life to cutting-edge fields. For example, in the manufacture of automotive sectors, drones, and humanoid robots, the integration of lightweight, high-strength, and high-toughness of polymer alloys is crucial yet still remains dispiriting. Moreover, the continuously variable adjustment of the totally new type of morphology for multicomponent polymers presented can be further extended to arbitrary engineering plastic commodities including polymethyl methacrylate (PMMA), polyphenylene oxide (PPO), polyvinylidene fluoride (PVDF) and polyethylene terephthalate (PET), represents a paradigm in accelerating the ongoing exploration and manufacture of advanced all-polymer materials. We believe this work will broaden the gaps between morphology and "tailor made" properties, and hold significant promise for the evolution of affordable plastic alloys with superior performance toward pilot plant scale, which is pursuing for long time by scientists.

Methods

Materials

Polyoxymethylene (POM, MC90, M_w=174300 g/mol, M_w/M_n= 2.19) used in this work were kindly provided by Shenhua Co., Ltd., China. Melt flow index is 9.23 g/10 min. Poly(L-lactide) (PLLA, 4032D, M_w=1.7×10^5 g/mol, M_w/M_n= 2.0) was supplied by Nature Works (USA). Ethylene-acrylic ester-glycidyl methacrylate terpolymer (EGMA, AX8900) was obtained from Arkema (France), which contains approximately 8 wt% GMA and 24 wt% methyl acrylates. N, N-dimethyl stearylamide (DMSA) utilized as a catalyst was purchased from Aladdin (USA).

Fabrication of "heterogeneous nano-domain (hDNs)"-structured alloys via melt processing

Before melt blending, PLLA and POM pellets were vacuum-dried at 80 ºC for 12 h, EGMA was dried at 60 ºC for 12 h. EGMA and PLLA were first melt-blended in a Haake internal mixer (Germany) at 190 ºC with a rotation speed of 50 rpm for 10 min, using DMSA as an efficient catalyst, to fabricate m-EGMA. The extent of in-situ reaction between EGMA and PLLA can be regulated by changing the weight ratio of EGMA/PLLA (from 10/1, 10/3, 10/5, 10/10, 10/15, 10/20, 10/25, to 10/30), as well as the concentration of DMSA (from 0wt%, 0.3wt%, 0.6wt%, 1.2wt%, to 2.4wt%). The obtained m-EGMA were then melt blended with POM at 190 ºC with a rotation speed of 50 rpm for 10 min to fabricate various POM-alloys. The obtained samples were injection-molded into standard specimens at a pressure of 550 MPa in a Haake Minijet Pro (Thermo Scientific, USA) at a barrel temperature of 200 ºC and a molding temperature of 80 ºC for mechanical tests. The samples into 0.5 mm thick sheets at 200 ºC for micromorphology observation and thermodynamic analysis.

Microstructure characterization

Gel content of m-EGMA were carried out by Soxhlet apparatus at 110 ºC for 36 h by the selective solvent of chloroform. The obtained insoluble products were dried for 24 h at 80 ºC in a vacuum oven. The gel fraction (f) was calculated via eq. 3,

$$gel\ fraction\ (\%)\ =\ (W_2/W_1)\ \times 100 \quad (3)$$

Here W_1 and W_2 refer to the weight of m-EGMA before and after selective extraction.

The morphologies of the specimens were observed by using Transmission Electron Microscopy (TEM) (Hitachi HT-7700) with a 100 kV accelerating voltage. The specimens were ultra cryo-microtomed (Leica EM UC7, Germany) equipped with a diamond knife (ultra 45º Diatome MT10514, Switzerland) to a thickness of 80 nm at -120 ºC and then stained by ruthenium tetroxide (RuO_4) at room temperature for 4 h in order to selectively stain the EGMA domains. The microstructures of all alloys were further observed by Scanning Electron Microscopy (SEM). Cryo-fractured surfaces and impact-fractured surfaces of blends were sputter-coated with a thin layer of gold and

then examined using a scanning electron microscope (FE-SEM, Hitachi S-4800), operating at an accelerating voltage of 3.0 kV. For the further exploration of POM alloys with AFM and nano-IR, laminates were fabricated via ultra cryo-microtome (Leica EM UC7, Germany) at -120 ºC. Approximately 100 nm of laminates were obtained and placed on silicon wafer for investigation. AFM and nano-IR measurements were carried out in AFM contact mode (Bruker nanoIR2-fs) with the scan rate of 0.5 Hz. The nano-IR imaging was conducted at the wavenumber of 931 cm^{-1}. The full IR spectra were collected from 3600 cm^{-1} to 900 cm^{-1} with 32 scans at a resolution of 2 cm^{-1}.

Performance characterization

Notched impact testing was conducted according to the GB/T 16420-1997 standard with an impact tester (SS-3700) and a pendulum energy of 2 J.

Tensile properties were measured using an Instron universal material testing system (model 5966) at a crosshead speed of 10 mm/min. Impact tests and tensile tests were all performed at room temperature. For each sample, the values reported here were averaged from six individual specimens.

A physical rheometer (MCR301, Anton Paar Instrument) with a parallel configuration (diameter 40 mm, gap 1 mm) was used for rheology characterization. The SAOS (small amplitude oscillatory shear) tests was performed at 190 ºC in a fixed amplitude (γ) of 5% after ensuring a linear viscoelastic (LVE) region. All tests were conducted in the frequency (ω) range from 500 to 0.01 rad/s. The plateau modulus was determined using Rouse correction using Rheoplus software from the obtained SAOS data. Thermo-gravimetric analysis (TGA) was performed using TGA Q500 (TA Instruments, USA) in an atmosphere of nitrogen. Approximately 5 mg of samples were placed in a sample tray at a heating rate of 10 ºC/min ranging from 30 ºC to 600 ºC.

Data availability

The authors declare that the data supporting the findings of this study are present within the article and its Supplementary Information file. Additional data related to the paper are available from the corresponding author upon request. Source data are provided with this paper.

References

1. Abbas-Abadi, M. S., Ureel, Y., Eschenbacher, A., Vermeire, F. H., Varghese, R. J., Oenema, J., Stefanidis, G.D. & Van Geem, K. M. Challenges and opportunities of light olefin production via thermal and catalytic pyrolysis of end-of-life polyolefins: Towards full recyclability. *Prog. Energ. Combust*. **96**, 101046 (2023).
2. Kabir, M. S., Wang, H., Luster-Teasley, S., Zhang, L. & Zhao, R. Microplastics in landfill leachate: Sources, detection, occurrence, and removal. *Environ. Sci. Ecotech*. **16**, 100256 (2023).
3. Zhou, L., Zhang, Z., Shi, C., Scoti, M., Barange, D. K., Gowda, R. R. & Chen, E. Y. X. Chemically circular, mechanically tough, and melt-processable polyhydroxyalkanoates. *Science* **380**, 64-69 (2023).
4. Chen, J., Wang, W., Zou, C., & Chen, C. Mechanical recycling of mixed plastics by supramolecular dynamic cross-linking strategy. *J. Am. Chem. Soc*. **147**,24747-24758 (2025).
5. Shi, H. H., Pan, Y., Xu, L., Feng, X., Wang, W., Potluri, P., Hu, L., Hasan, T. & Huang, Y. Y. S. Sustainable electronic textiles towards scalable commercialization. *Nat. Mater*. **22**, 1294-1303 (2023).
6. Xiao, Y., Lian, X., Sun, Y., Sung, Y. C., Vaidya, A., Chen, Z., Gupta, A., Chatterjee, S., Zheng, L., Guerrero, E., Wang, X., Farbiak, L., Yang, Y., Diamond, M. I., Leal, C., McDonald, J. G. & Siegwart, D. J. High-density brush-shaped polymer lipids reduce anti-PEG antibody binding for repeated administration of mRNA therapeutics. *Nat. Mater*. **24**, 1840-1851 (2025).
7. Wang, H., Yang, M., Tang, Q., Zhao, X., Tong, Y. & Liu, Y. Flexible, conformal organic synaptic transistors on elastomer for biomedical applications. *Adv. Funct. Mater*. **29**, 1901107 (2019).
8. Anguita, J. V., Smith, C. T. G., Stute, T., Funke, M., Delkowski, M. & Silva, S. R. P. Dimensionally and environmentally ultra-stable polymer composites reinforced with carbon fibres. *Nat. Mater*. **19**, 317-322 (2020).
9. Hassan, M., Mohanty, A. K. & Misra, M. Additive Manufacturing of a super toughened

biodegradable polymer blend: Structure-property-processing correlation and 3D printed prosthetic part development. *ACS Appl. Polym. Mater*. **6**, 3849-3863 (2024).

10. Arico, A. S., Bruce, P., Scrosati, B., Tarascon, J. M. & Van Schalkwijk, W. Nanostructured materials for advanced energy conversion and storage devices. *Nat. Mater*. **4**, 366-377 (2005).
11. Wang, J., Zhang, X., Jiang, L. & Qiao, J. Advances in toughened polymer materials by structured rubber particles. *Prog. Polym. Sci*. **98**, 101160 (2019).
12. Eagan, J. M., Xu, J., Di Girolamo, R., Thurber, C. M., Macosko, C. W., LaPointe, A. M., Bates, F. S. & Coates, G. W. Combining polyethylene and polypropylene: Enhanced performance with PE/i PP multiblock polymers. *Science* **355**, 814-816 (2017).
13. Cater, H. L., Allen, M. J., Linnell, M. I., Rylski, A. K., Wu, Y., Lien, H. M., Mangolini, F., Freeman, B. D. & Page, Z. A. Supersoft norbornene‐based thermoplastic elastomers with high strength and upper service temperature. *Adv. Mater*. **36**, 2402431 (2024).
14. Gao, C., Chenchai, K., Huang, L., Li, C., Zhang, X., Zhang, G., Shao, J., Zhang, H., Liu, G., Hou, Z. & Zhang, D. Polymer semiconductor blends with remarkably stable semiconducting performance under large and cyclic mechanical deformation. *Nat. Commun*. **16**, 10388 (2025).
15. Qi, X., Huang, X., Kanwal, N., Das, B., Phillips, A. E., Papageorgiou, D. G., Yan, H., Bilotti, E. & Reece, M. J. High entropy engineered polymer blends with enhanced dielectric properties and high temperature stability. *Nat. Commun*. **16**, 9056 (2025).
16. Chen, J., Pei, Z., Chai, B., Jiang, P., Ma, L., Zhu, L. & Huang, X. Engineering the dielectric constants of polymers: from molecular to mesoscopic scales. *Adv. Mater*. **36**, 2308670 (2024).
17. Clarke, R. W., Sandmeier, T., Franklin, K. A., Reich, D., Zhang, X., Vengallur, N., Patra, T. K., Tannenbaum, R. J., Adhikari, S., Kumar, S. K., Rovis, T. & Chen, E. Y. X. Dynamic crosslinking compatibilizes immiscible mixed plastics. *Nature* **616**, 731-739 (2023).
18. Liu, Y., Wan, J., Zhao, X., Zhao, J., Guo, Y., Bai, R., Zhang, Z. Yu, W., Gibson, H. W. & Yan, X. Highly strong and tough supramolecular polymer networks enabled by cryptand-based host-guest recognition. *Angew. Chem. Int. Edit*. **62**, e202302370 (2023).

19. Yang, D. D., Wu, C., Wu, G., Chen, S. C. & Wang, Y. Z. Toughening of polylactide with high tensile strength via constructing an integrative physical crosslinking network based on ionic interactions. *Macromolecules* **54**, 291-301 (2020).

20. Guan, Y., Tu, L., Ren, K., Kang, X., Tian, Y., Deng, W., Yu, P., Ning, C., Fu, R., Tan, G. & Zhou, L. Soft, super-elastic, all-polymer piezoelectric elastomer for artificial electronic skin. *ACS Appl. Mater. Inter*. **15**, 1736-1747 (2022).

21. White, T. J., & Broer, D. J. Programmable and adaptive mechanics with liquid crystal polymer networks and elastomers. *Nat. Mater*. **14**, 1087-1098 (2015).

22. Zhou, X., Sheng, Y., Chen, G., Wan, H., Lu, L., Xing, H., Huang, J. Zhu, Z. Wang, Y., Bao, H., Wu, J., Zhao, Q. Xie, T. & Zheng, N. Geometrically insensitive deform-and-go liquid crystal elastomer actuators through controlled radical diffusion. *Nat. Commun*. **16**, 7536 (2025).

23. Huang, J., Zhang, X., Liu, R., Ding, Y. & Guo, D. Polyvinyl chloride-based dielectric elastomer with high permittivity and low viscoelasticity for actuation and sensing. *Nat. Commun*. **14**, 1483 (2023).

24. Amoli, V., Kim, J. S., Jee, E., Chung, Y. S., Kim, S. Y., Koo, J., Choi, H., Kim, Y. & Kim, D. H. A bioinspired hydrogen bond-triggered ultrasensitive ionic mechanoreceptor skin. *Nat. Commun*. **10**, 4019 (2019).

25. Grau, G., Frazier, E. J. & Subramanian, V. Printed unmanned aerial vehicles using paper-based electroactive polymer actuators and organic ion gel transistors. *Microsyst. Nanoeng*. **2**, 1-8 (2016).

26. Leibler, L. Nanostructured plastics: Joys of self-assembling. *Prog. Polym. Sci*. **30**, 898-914 (2005).

27. Ruzette, A. V. & Leibler, L. Block copolymers in tomorrow's plastics. *Nat. Mater*. **4**, 19-31 (2005).

28. Stratigaki, M., Baumann, C. & Göstl, R. Confocal microscopy visualizes particle–crack interactions in epoxy composites with optical force probe-cross-linked rubber particles. *Macromolecules* **55**, 1060-1066 (2022).

29. Chen, X., Zeng, Z., Ju, Y., Zhou, M., Bai, H. & Fu, Q. Design of biodegradable PLA/PBAT

blends with balanced toughness and strength via interfacial compatibilization and dynamic vulcanization. *Polymer* **266**, 125620 (2023).

30. Gao, Y., Jiang, Z., Zhang, J., Tan, H., Jin, J. & Jiang, W. Models and theories regarding the brittle-ductile transition of rubber-toughened thermoplastics and their application in the design of high-impact polymer composites with Balanced Toughness and Rigidity. *Polym. Sci. Technol*. **1**, 314-329 (2025).
31. Pernot, H., Baumert, M., Court, F. & Leibler, L. Design and properties of co-continuous nanostructured polymers by reactive blending. *Nat. Mater*. **1**, 54-58 (2002).
32. Jin, B. & Yang, S. Programming liquid crystalline elastomer networks with dynamic covalent bonds. *Adv. Funct. Mater*. **33**, 2304769 (2023).
33. Yang, R., Cai, C., Han, X., Chen, Z., Gu, G., Zhang, C., Zou, G. & Li, J. Supertough and biodegradable poly (lactic acid) blends with “hard-soft” core-shell unsaturated poly (ether-ester) through self-vulcanization. *Macromolecules* **56**, 7271-7285 (2023).
34. Qu, Y., Hong, J., Chen, Y., Ling, X., Wu, J., Wang, H. & Li, Y. Rigid molecular chains trapped reactive elastomers for high performance PLLA composites with excellent tough-strength balance. *Compos. Part B-Eng*. **255**, 110619 (2023).
35. Wang, X., Gao, Y., Jin, J. & Jiang, W. A strategy to develop homo-polypropylene composites with high impact and high rigidity. *Macromolecules* **57**, 4576-4583 (2024).
36. Crevecoeur, G., Ph.D. thesis, Katholieke Universiteit, Leuven, Belgium (1991).
37. Nir, M. M., Ram, A. & Miltz, J. Performance of reprocessed multilayer LDPE/nylon‐6 film. *Polym. Eng. Sci*. **35**, 1878-1883 (1995).
38. Wang, H., Chen, J. & Li, Y. Arrested elongated interface with small curvature by the simultaneous reactive compatibilization and stereocomplexation. *Macromolecules* **53**, 10664-10674 (2020).
39. Liu, H., Chen, N., Peng, C., Zhang, S., Liu, T., Song, P., Zhong, G. & Liu, H. Diisocyanate-induced dynamic vulcanization of difunctional fatty acids toward mechanically robust PLA blends with enhanced luminescence emission. *Macromolecules* **55**, 7695-7710 (2022).
40. Wang, J., Reyna-Valencia, A. & Favis, B. D. Assembling conductive PEBA copolymer at the continuous interface in ternary polymer systems: morphology and resistivity.

Macromolecules **49**, 5115-5125 (2016).

41. Seo, Y., Hwang, S. S., Kim, K. U., Lee, J. & Hong II, S. Influence of the mechanical properties of the dispersed phase upon the behaviour of nylon/rubber blends: crosslinking effect. *Polymer* **34**, 1667-1676 (1993).
42. Borggreve, R. J. M., Ph.D. thesis, Twente University of Technology, The Netherlands (1986).
43. Wu, S. Phase structure and adhesion in polymer blends: a criterion for rubber toughening. *Polymer* **26**, 1855-1863 (1985).
44. Yokoyama, K. & Guan, Z. A vitrimer acts as a compatibilizer for polyethylene and polypropylene blends. *Angew. Chem. Int. Edit*. **136**, e202317264 (2024).
45. Machiels, A. G. C., Denys, K. F. J., Van Dam, J. & De Boer, A. P. Effect of processing history on the morphology and properties of polypropylene/thermotropic liquid crystalline polymer blends. *Polym. Eng. Sci*. **37**, 59-72 (1997).
46. Wang, W., Luo, J., Wang, X. & Wang, Z. Tensile Deformation above the Glass Transition Temperature to Construct a Crystalline Microfibrillar Superstructure for Achieving Supertough, Ultrastrong, and Transparent Neat Polylactide. *Macromolecules* **58**, 4419-4437 (2025).
47. Zeng, D. & Hayward, R. C. Effects of randomly end-linked copolymer network parameters on the formation of disordered cocontinuous phases. *Macromolecules* **52**, 2642-2650 (2019).
48. Banerji, A., Jin, K., Mahanthappa, M. K., Bates, F. S. & Ellison, C. J. Porous fibers templated by melt blowing cocontinuous immiscible polymer blends. *ACS Macro Lett*. **10**, 1196-1203 (2021).
49. Trifkovic, M., Hedegaard, A., Huston, K., Sheikhzadeh, M. & Macosko, C. W. Porous films via PE/PEO cocontinuous blends. *Macromolecules* **45**, 6036-6044 (2012).
50. Chen, J., Rong, C., Lin, T., Chen, Y., Wu, J., You, J., Wang, H. & Li, Y. Stable co-continuous PLA/PBAT blends compatibilized by interfacial stereocomplex crystallites: toward full biodegradable polymer blends with simultaneously enhanced mechanical properties and crystallization rates. *Macromolecules* **54**, 2852-2861 (2021).
51. Ye, H., Li, C., Zhang, Y., Xia, Y., Wang, H. & Li, Y. Formation of an organic rigid core–soft

shell structure based on the melting temperature difference between the core and the matrix by reactive processing: A facile strategy for highly efficient polymer toughening. *Macromolecules* **58**, 1223-1234 (2025).

52. Ye, H., Li, A., Li, G., Li, K., Zhang, J., Wang, D., Ray, S. S., Wang, H. & Li, Y. Construction of elastomeric nanobelts in a glassy polymer matrix: toward supertoughened nanoalloys with significantly depressed yielding behaviors. *Macromolecules* **57**, 9999-10015 (2024).
53. Qu, Y., Chen, Y., Ling, X., Wu, J., Hong, J., Wang, H. & Li, Y. Reactive micro-crosslinked elastomer for supertoughened polylactide. *Macromolecules* **55**, 7711-7723 (2022).
54. Qiu, J., Xing, C., Cao, X., Wang, H., Wang, L., Zhao, L. & Li, Y. Miscibility and double glass transition temperature depression of poly (l-lactic acid)(PLLA)/poly (oxymethylene)(POM) blends. *Macromolecules* **46**, 5806-5814 (2013).
55. Ye, L., Shi, X., Ye, C., Chen, Z., Zeng, M., You, J. & Li, Y. Crystallization-modulated nanoporous polymeric materials with hierarchical patterned surfaces and 3D interpenetrated internal channels. *ACS Appl. Mater. Inter*. **7**, 6946-6954 (2015).
56. Ye, L., Qiu, J., Wu, T., Shi, X. & Li, Y. Banded spherulite templated three-dimensional interpenetrated nanoporous materials. *RSC Adv*. **4**, 43351-43356 (2014).
57. Feng, Y., Zhao, G., Yin, J. & Jiang, W. Reactive compatibilization of high‐impact poly (lactic acid)/ethylene copolymer blends catalyzed by N, N‐dimethylstearylamine. *Polym. Int*. **63**, 1263-1269 (2014).
58. Ye, L., Ye, C., Xie, K., Shi, X., You, J. & Li, Y. Morphologies and crystallization behaviors in melt-miscible crystalline/crystalline blends with close melting temperatures but different crystallization kinetics. *Macromolecules* **48**, 8515-8525 (2015).
59 Trent, J. S., Scheinbeim, J. I. & Couchman, P. R. Ruthenium tetraoxide staining of polymers for electron microscopy. *Macromolecules* **16**, 589-598 (1983).
60 Sun, A., Luo, F., Chen, R., Shih, T. M. & Guo, S. Toward supertough and heat-resistant binary blend: polyoxymethylene/elastomer via in-situ graft copolymer formation during one-pot reactive melt blending. *J. Polym. Res*. **30**, 101 (2023).
61. Mohsenzadeh, R., Soudmand, B. H. & Shelesh‐Nezhad, K. Synergetic impacts of two rigid nano-scale inclusions on the mechanical and thermal performance of POM/carbon

black/$CaCO_3$ ternary nanocomposite systems. *Polym. Composites* **43**, 3041-3056 (2022).

62. Babar, S., Ebenezer, K., Mishra, D., Patil, H. B., Nikam, P. & Rao, A. R. Synthesis of castor oil-based glycidyl carbamate polyurethane elastomer and its effect on toughening of polyoxymethylene. *J. Mater. Sci*. **58**, 7209-7226 (2023).
63. Huang, C. Y. & Tseng, C. I. The effect of interface modification between POM and PTFE on the properties of POM/PTFE composites. *J. Appl. Polym. Sci*. **78**, 800-807 (2000).
64. Kang, X., Liu, Y., Chen, N., Feng, W., Liu, B., Xu, Y., Li, J., Ding, T. & Fang, X. Influence of modified ammonium polyphosphate on the fire behavior and mechanical properties of polyformaldehyde. *J. Appl. Polym. Sci*. **138**, 50156 (2021).
65. Zhang, L., Zhuo, X., Shi, H., Yu, S., Tian, H., Chen, J., Hao, Y., Chen, L., Liu, W. & Xie, Y. Effects of glass fiber reinforcing and thermal post-reatment on the mechanical properties and crystallization behaviors of polyoxymethylene. *J. Appl. Polym. Sci*. **140**, 1-11 (2023).
66. Song, Z., Huang, X., Lu, X., Lv, Q., Xu, N., Pang, S., Pan, L. & Li, T. Improvement of microstructures and properties of poly (lactic acid)/poly (ε-caprolactone) blends compatibilized with polyoxymethylene. *J. Appl. Polym. Sci*. **135**, 46536 (2018).
67. Qian, Z., Wang, Y., Li, J., Wang, X. & Wu, D. Development of sustainable polyoxymethylene-based composites with recycled carbon fibre: mechanical enhancement, morphology, and crystallization kinetics. *J. Reinf. Plast. Comp*. **33**, 294-309 (2014).
68. Andrzejewski, J., Skórczewska, K. & Kloziński, A. Improving the toughness and thermal resistance of polyoxymethylene/poly (lactic acid) blends: Evaluation of structure‐properties correlation for reactive processing. *Polymers* **12**, 307 (2020).
69. Rustamov, I., Xiang, L., Xia, Y. & Peng, W. Tribological and mechanical endowments of polyoxymethylene by liquid‐phase exfoliated graphene nanofiller. *Polym. Int*. **74**, 231-245 (2025).
70. Zhao, X. & Ye, L. Study on the thermal conductive polyoxymethylene/graphite composites. *J. Appl. Polym. Sci*. **111**, 759-767 (2009).
71. Bai, S. & Wang, Q. Effect of injection speed on phase morphology, crystallization behavior, and mechanical properties of polyoxymethylene/poly (ethylene oxide) crystalline/crystalline blend in injection processing. *Polym. Eng. Sci*. **52**, 1938-1944 (2012).

72. Yang, J., Yang, W., Wang, X., Dong, M., Liu, H., Wujcik, E. K., Shao, W., Wu, S., Ding, T. & Guo, Z. Synergistically toughening polyoxymethylene by methyl methacrylate-butadiene-styrene copolymer and thermoplastic polyurethane. *Macromol. Chem. Phys*. **220**, 1800567 (2019).

73. Chang, F. C. & Yang, M. Y. Mechanical fracture behavior of polyacetal and thermoplastic polyurethane elastomer toughened polyacetal. *Polym. Eng. Sci*. **30**, 543-552 (1990).

74. Cheng, Z., & Wang, Q. Morphology control of polyoxy-methylene/thermoplastic polyurethane blends by adjusting their viscosity ratio. *Polym. Int*. **55**, 1075-1080 (2006).

75. Ren, X. C., Chen, L., Zhao, H. J., Dan, Y. & Cai, X. F. Acrylate elastomer toughened and UV stabilized polyoxymethylene. *J. Macromol. Sci. B*. **46**, 411-421 (2007).

76. Choi, H., Song, Y. S. & Suh, D. Comprehensive rheological characterization of polynucleotide/BDDE-crosslinked hyaluronic acid blend for intra-articular viscosupplementation. *Sci. Rep*. **15**, 38185 (2025).

77. Qiao, H., Zheng, B., Zhong, G., Li, Z., Cardinaels, R., Moldenaers, P., Lamnawar, K., Maazouz, A., Liu, C. & Zhang, H. Understanding the rheology of polymer‐polymer interfaces covered with Janus nanoparticles: Polymer blends versus particle sandwiched multilayers. *Macromolecules* **56**, 647-663 (2023).

78. Shah, R. S., Bryant, S. & Trifkovic, M. Microstructural rearrangements and their rheological signature in coarsening of cocontinuous polymer blends. *Macromolecules* **53**, 10918-10926 (2020).

79. Susa, A., Bose, R. K., Grande, A. M., van der Zwaag, S. & Garcia, S. J. Effect of the dianhydride/branched diamine ratio on the architecture and room temperature healing behavior of polyetherimides. *ACS Appl. Mater. Inter*. **8**, 34068-34079 (2016).

80. Pötschke, P. & Paul, D. R. Formation of co-continuous structures in melt-mixed immiscible polymer blends. *J. Macromol. Sci. C* **43**, 87-141 (2003).

81. Guo, H. F., Packirisamy, S., Mani, R. S., Aronson, C. L., Gvozdic, N. V. & Meier, D. J. Compatibilizing effects of block copolymers in low-density polyethylene/polystyrene blends. *Polymer* **39**, 2495-2505 (1998).

Acknowledgements

This work was financially supported by the

Author contributions

Author 1 conceived this study and designed the architectures, performed TEM experiments, analyzed data and wrote the manuscript with input from all authors. Author 2 conducted the structural design, fabrication, characterizations and data analysis. Author 3 helped to fabricate the alloys and performed the mechanical experiment. Author 4 contributed to the analysis of spectroscopy data and revision of the manuscript. Author 5 supervised the project, analyzed data, co-wrote the paper and acquired the funding. All authors discussed the results and commented on the manuscript.

Competing interests

The authors declare no competing interests.

Additional information

Supplementary information The online version contains supplementary material available at http://doi.

Correspondence and requests for materials should be addressed to Dr. 1 or Prof. 5.

Peer review information *Nature Communications* thanks to A and the other anonymous reviewers for their contribution to the peer review of this work. A peer review file is available.

Reprints and permissions information is available at www. nature.com/reprints.

Publisher's note Springer Nature remains neutral with regard to jurisdictional claims in published maps and institutional affiliations.

Open Access This article is licensed under a Creative Commons Attribution-NonCommercial-NoDerivatives 4.0 International License, which permits any non-commercial use, sharing, distribution and reproduction in any medium or format, as long as you give appropriate credit to the original author(s) and the source, provide a link to the Creative Commons licence, and indicate if you modified the licensed material. You do not have permission under this licence to

share adapted material derived from this article or parts of it. The images or other third party material in this article are included in the article's Creative Commons licence, unless indicated otherwise in a credit line to the material. If material is not included in the article's Creative Commons licence and your intended use is not permitted by statutory regulation or exceeds the permitted use, you will need to obtain permission directly from the copyright holder. To view a copy of this licence, visit http:// creativecommons.org/licenses/by-nc-nd/4.0/.

Supplementary Files

This is a list of supplementary files associated with this preprint. Click to download.

- 2SI20260225.docx